The Astrophysical Journal Supplement Series, 210:18 (9pp), 2014 February doi:10.1088/0067-0049/210/2/18

THE GALACTIC BULGE SURVEY: COMPLETION OF THE X-RAY SURVEY OBSERVATIONS

Peter G. Jonker[1,2,3], Manuel A. P. Torres[1,3], Robert I. Hynes[4], Thomas J. Maccarone[5], Danny Steeghs[6], Sandra Greiss[6], Christopher T. Britt[4,5], Jianfeng Wu[3], Christopher B. Johnson[4], Gijs Nelemans[2,7], and Craig Heinke[8]

[1] SRON, Netherlands Institute for Space Research, Sorbonnelaan 2, 3584-CA, Utrecht, The Netherlands
[2] Department of Astrophysics/IMAPP, Radboud University Nijmegen, Heyendaalseweg 135, 6525-AJ, Nijmegen, The Netherlands
[3] Harvard–Smithsonian Center for Astrophysics, 60 Garden Street, Cambridge, MA 02138, USA
[4] Department of Physics and Astronomy, Louisiana State University, Baton Rouge, LA 70803-4001, USA
[5] Department of Physics, Texas Tech University, P.O. Box 41051, Lubbock, TX 79409-1051, USA
[6] Astronomy and Astrophysics, Department of Physics, University of Warwick, Coventry CV4 7AL, UK
[7] Institute for Astronomy, KU Leuven, Celestijnenlaan 200D, B-3001, Leuven, Belgium
[8] Department of Physics, University of Alberta, Room 238 CEB, Edmonton AB T6G 2G7, Canada
Received 2013 December 2; accepted 2013 December 11; published 2014 January 10

ABSTRACT

We provide the *Chandra* source list for the last ∼quarter of the area covered by the Galactic Bulge Survey (GBS). The GBS targets two strips of $6^\circ \times 1^\circ$ (12 square degrees in total), one above ($1^\circ < b < 2^\circ$) and one below ($-2^\circ < b < -1^\circ$) the Galactic plane in the direction of the Galactic center at X-ray, optical, and near-infrared wavelengths. For the X-ray part of the survey we use 2 ks per *Chandra* pointing. We find 424 X-ray sources in the 63 *Chandra* observations on which we report here. These sources are in addition to the 1216 X-ray sources discovered in the first part of the GBS survey described previously. We discuss the characteristics and the X-ray variability of the brightest of the sources as well as the radio properties from existing radio surveys. We point out an interesting asymmetry in the number of X-ray sources as a function of their Galactic *l* and *b* coordinates which is probably caused by differences in average extinction toward the different parts of the GBS survey area.

Key words: accretion, accretion disks – binaries: symbiotic – novae, cataclysmic variables – stars: activity – X-rays: binaries

Online-only material: color figures, machine-readable table

1. INTRODUCTION

Stellar mass black holes and neutron stars are the end points of massive star evolution via supernovae or gamma-ray bursts. Nearly all of the Galactic black holes and many of the neutron stars found so far are located in binaries. Their properties are the observable consequences of binary interactions. Studying these remnants provides vital clues to understanding the evolutionary processes that produce them both in terms of single massive star evolution and binary star evolution. For example, the current stellar mass black hole distribution based on a sample of about 20 objects appears to be disjoint from that of neutron stars (Özel et al. 2010, 2012; Farr et al. 2011) suggesting a bimodality in formation that produces either low-mass neutron stars or relatively high-mass black holes, with few systems in between. This remains a challenge for supernova models to reproduce (Fryer et al. 2012; Belczynski et al. 2012). Kreidberg et al. (2012) argue that this mass gap may be due, in part, to systematic effects underestimating the system inclination.

Unfortunately, our observational sample, particularly in the case of black holes, is largely comprised of objects discovered in transient X-ray outbursts, leading to a variety of possible selection effects that could obscure the properties of the true population (e.g., see Narayan & McClintock 2005). For instance, using the disk instability model including disk irradiation effects (see Lasota 2008), one could envisage an inverse correlation between the accretor mass and the duty cycle, reducing the chance of detection of relatively low-mass black holes in outbursts. Additional selection effects could be invoked by the black-hole-mass–orbital-period correlation (Lee et al. 2002) and, possibly related to that, the optical and X-ray outburst peak-luminosity–orbital-period correlation (Shahbaz & Kuulkers 1998 and Wu et al. 2010, respectively).

To mitigate the selection effects incurred by selecting systems that recently went through an outburst cycle we designed the Galactic Bulge Survey (GBS; Jonker et al. 2011). The GBS is a wide, shallow *Chandra* X-ray survey of the Galactic Bulge aiming to uncover many (>100) new *quiescent* black hole and neutron star binaries. As a result, we may find sources quite different from those identified in outbursts. A second goal of the survey is to constrain binary evolution models (e.g., King & Ritter 1999; Pfahl et al. 2002; Belczynski & Taam 2004) using the observed number ratio between the ≈100 X-ray binaries and several hundred CVs that we expect to find. This number will particularly put constraints on uncertain phases in the binary evolution such as the common envelope phase (e.g., Kiel & Hurley 2006; Ivanova et al. 2013).

For both these science goals we need to classify the X-ray sources. Given that this classification relies on multi-wavelength data, by design, the survey area is sufficiently out of the plane to allow (multi-epoch) optical and near-infrared (NIR) follow-up of the majority of detected sources. In addition to classification, optical and NIR spectroscopic observations are also crucial for dynamical studies to derive compact object masses (and sometimes the dynamical masses are necessary for classification, e.g., Ratti et al. 2013).

The GBS is well under way. Radio counterparts of a sample of sources from the first part of the X-ray survey have been identified by Maccarone et al. (2012). Hynes et al. (2012) reported on associations of X-ray sources with the brightest optical counterparts. Results from optical variability alone (Udalski et al. 2012) and optical variability and spectroscopic

studies together (Ratti et al. 2013; Britt et al. 2013; Hynes et al. 2014; Torres et al. 2013) are appearing. Furthermore, we are using NIR observations from the Two Micron All Sky Survey (2MASS), VISTA Variables in The Via Lactea (VVV), and the UKIRT Infrared Deep Sky Survey to identify counterparts of the GBS X-ray sources (Greiss et al. 2014).

Here we report on *Chandra* observations of the final ≈quarter of the sky area of 12 square degrees that makes up the GBS, completing the *Chandra* survey observations of the GBS area. The initial three quarters were reported in Jonker et al. (2011). In addition, we provide the radio counterparts to the X-ray sources discovered in the final part after Maccarone et al. (2012) reported on archival radio sources for the first three quarters. Finally, we investigate the spatial distribution of all the X-ray sources found in the GBS area, and by comparing these with the *ROSAT* sources in the sky area on which we report here, we investigate the variability properties of the new GBS X-ray sources.

2. *CHANDRA* X-RAY OBSERVATIONS, ANALYSIS, AND RESULTS

2.1. Source Detection

We have obtained 63 observations with the *Chandra X-Ray Observatory* (Weisskopf et al. 2002) covering the remaining quarter of the total area of 12 square degrees that we call the GBS. We employed the same analysis tools and techniques as described in Jonker et al. (2011) as much as possible in order to come to as homogeneous a survey as possible. Also we follow the source naming convention introduced there, where sources reported in Jonker et al. (2011) are referred to as CX# (after *Chandra* X-ray source, where the numeral indicates the position of that source in the list, with sources providing the largest number of counts at detection having the lowest numeral), while new sources found in the 63 new observations are called CXB#.

In the left panel in Figure 1 we show the 63 new *Chandra* observations reported on here. The red curved line indicates the composite outline of each circular field of view of 14′ diameter for these 63 observations. The gray curved lines bordering the white points indicate the composite outline of each circular field of view of 14′ diameter of the individual *Chandra* observations obtained and the detected sources reported in Jonker et al. (2011), respectively. The area near $l = 0^\circ$ is covered by the observations from Hong et al. (2009). Sources found in 2 ks segments of those exposures were listed in Jonker et al. (2011) as well. In the right panel in Figure 1 the white circles indicate the position of the detected point sources. The size of the white circles is an indication of the number of *Chandra* counts detected for that particular source.

The *Chandra* observations have been performed using the I0–I3 CCDs of the Advanced CCD Imaging Spectrometer (ACIS) detector (Garmire 1997; ACIS-I). The observation identification (ID) numbers for the data presented here are 13528–13590. We reprocessed and analyzed the data using the CIAO 4.3 software developed by the *Chandra* X-ray Center and employing CALDB version 4.4.6. The data telemetry mode was set to very faint for all observations. The very faint mode provides 5 × 5 pixel information per X-ray event. This allows for a better screening of events caused by cosmic rays. In our analysis we selected events only if their energy falls in the 0.3–8 keV range.

We used WAVDETECT to search for X-ray sources in each of the observations using data covering the full 0.3–8, the 0.3–2.5, and the 2.5–8 keV energy bands, separately. We set the SIGTHRESH in WAVDETECT to 1×10^{-7}, which implies that for a background count rate constant over the ACIS-I CCDs there would be <0.1 spurious source detection per observation as about 1×10^6 pixels are searched per observation. However, in most cases a source is not detected in a single pixel, thus our estimate of 0.1 spurious source per observation is very conservative. Furthermore, as we explain below, we applied additional selection criteria. This further lowers the number of spurious sources.

We retained all sources for which Poisson statistics indicate that the probability of obtaining the number of detected source counts by chance, given the expectation for the local background count rate, is lower than 1×10^{-6}. This would be equivalent to a $>5\sigma$ source detection in Gaussian statistics. Next, we deleted all sources for which WAVDETECT was not able to provide an estimate of the uncertainty on the right ascension (α) and on declination (δ) as this often indicates that all counts fell in 1 pixel which could well be due to faint afterglow events caused by cosmic-ray hits. In addition, we impose a three count minimum for source detection as Murray et al. (2005) simulated that in their XBootes survey with 5 ks ACIS-I exposures, 14% of the two-count sources were spurious (note that this percentage will probably be lower for our GBS exposures of 2 ks).

Since our *Chandra* observations were designed to overlap near the edges, we searched for multiple detections of the same source either in one of the energy sub-bands or in the full energy band. We consider sources with positions falling within 5″ of each other likely multiple detections of the same source. This radius is larger than that of 3″ which we took in Jonker et al. (2011) as we found out that some multiple detections of the same source still remained for sources detected with large off-axis angles (see Hynes et al. 2012 for the list of 18 sources from Jonker et al. 2011 that were in fact multiple detections of the same source.) This means that in Jonker et al. (2011) we found 1216 unique sources.

In the last quarter of the GBS area that we report on here, we found that 26 sources are detected more than once. Out of these 26 sources, 23 sources are detected two times, and 3 sources are detected three times. Two of the sources detected twice were already detected and reported in Jonker et al. (2011; CX155 and CX314). We do not list these two sources in Table 1. The properties that we list in Table 1 for the sources that are detected multiple times are those for the detection that gave rise to the largest number of X-ray counts. In Table 1 we also list the number of times that sources are detected.

Besides the multiple detections of CX155 and CX314, 14 additional sources detected once in the cycle 13 *Chandra* observations were previously detected and listed in Jonker et al. (2011). These sources are CX15, CX17, CX25, CX44, CX60, CX69, CX79, CX137, CX221, CX266, CX312, CX355, CX374, and CX439. In most cases the off-axis angle of the source position was larger during the new observations and, given that a similar number of X-ray counts was detected in each instance, the source position provided in Jonker et al. (2011) is the most accurate X-ray position available. The main exception where we consider the newly derived position to be more accurate is CX314. CX314 was detected at 10.′8 off-axis at eight counts in the *Chandra* detection leading to its discovery. The new detection we report on here provides 17 counts and the source was 5.′9 off-axis in ObsID 13581. The new best-fit source position is $(\alpha, \delta) = (266.6461515, -31.8136964)$ which is 2.″6 from the previously reported position.

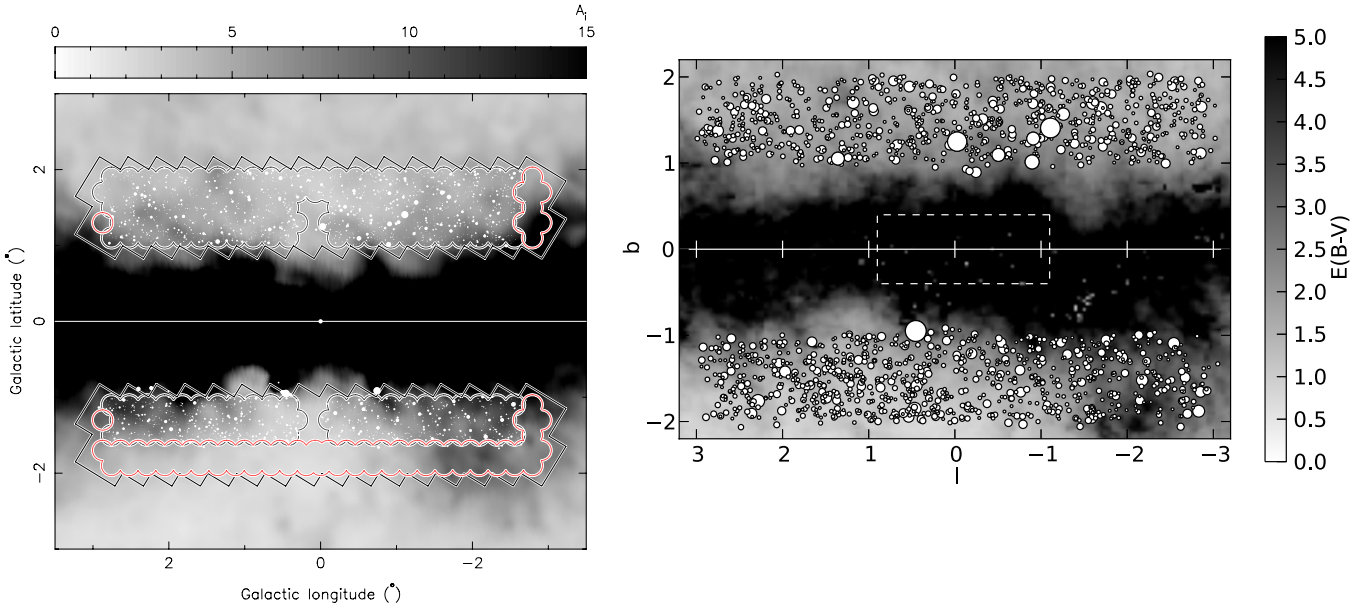

Figure 1. Left panel: the large black, white-rimmed saw-tooth boxes are the outline of our optical observations of the GBS area in Galactic coordinates. The gray-scale image depicts the total reddening in the Sloan i'-band filter, $A_{i'}$, estimated from the *COBE* dust maps (Schlegel et al. 1998). The overplotted white circles indicate the position of the *Chandra* X-ray sources detected in the GBS reported in Jonker et al. (2011). The sources found in the areas near $l = 0°$ and $1° < |b| < 2°$ were reported in Jonker et al. (2011) but the observations were from Hong et al. (2009). The red-rimmed curved lines indicate the composite outline of each circular field of view of 14′ diameter for the 63 *Chandra* observations that we report on in this paper. Right panel: the gray-scale image and contours depict the total absorption $E(B-V)$, estimated from the extinction maps from the VVV (Gonzalez et al. 2012). The overplotted white circles indicate the position of all X-ray sources detected in the GBS including the new sources reported on here. The size of the white circles is proportional to the number of *Chandra* counts detected for that particular source. The dashed rectangle outlines the region of the survey of the Galactic center from Wang et al. (2002).

Table 1
The GBS X-Ray Source List Providing the GBS Source Name

Source Name	CXB#	α (degrees)	δ (degrees)	$\Delta\alpha$ (″)	$\Delta\delta$ (″)	# (cnt)	Obs ID	Off-axis Angle (′)	# of Detec.	Δpos (″)	HR
CXOGBSJ175748.7−275214	CXB1	269.4529160	−27.8707194	0.19	0.22	161	13536	7.74	1	0.74	-0.61 ± 0.06
CXOGBSJ175359.8−292907	CXB2	268.4994759	−29.4852781	0.09	0.05	148	13550	4.35	2	0.35	-0.18 ± 0.02
CXOGBSJ174614.3−321949	CXB3	266.5599883	−32.3303786	0.06	0.05	105	13574	2.64	1	0.31	0.28 ± 0.03
CXOGBSJ173416.2−304538	CXB4	263.5678548	−30.7607505	0.15	0.09	70	13586	3.78	1	0.51	-0.90 ± 0.12
CXOGBSJ173208.6−302828	CXB5	263.0362304	−30.4746348	0.07	0.10	66	13587	3.78	1	0.53	-0.75 ± 0.10
CXOGBSJ174517.0−321356	CXB6	266.3208565	−32.2323620	0.11	0.11	66	13577	3.73	2	0.52	0.78 ± 0.11
CXOGBSJ175551.6−283213	CXB7	268.9650346	−28.5369772	0.06	0.05	65	13533	1.83	1	0.32	0.34 ± 0.05
CXOGBSJ175432.1−292824	CXB8	268.6339299	−29.4734138	0.28	0.26	65	13550	7.49	2	1.42	-0.78 ± 0.11
CXOGBSJ174916.6−311518	CXB9	267.3192034	−31.2550666	0.09	0.07	64	13569	3.52	1	0.50	-0.95 ± 0.13
CXOGBSJ175832.4−275244	CXB10	269.6350093	−27.8789043	0.13	0.11	53	13558	4.30	1	0.68	-0.56 ± 0.09

Notes. The source number as used in this paper is preceded by "CXB" to differentiate it from the sources in Jonker et al. (2011)), α, δ in decimal degrees, the 3σ error on localizing the source on the detector α and δ in arcseconds, the total number of counts detected, the ID of the observation resulting in the detection, the off-axis angle at which the source is detected, the number of times the source was detected in the *Chandra* observations, the 95% confidence positional uncertainty (Δpos) calculated according to formula (4) in Evans et al. (2010) taking the boresight uncertainty into account, and the hardness ratio (HR) for sources detected with more than 20 counts. The hardness is defined as the ratio between the count rate in the 2.5–8 keV minus that in the 0.3–2.5 keV band to the count rate in the full 0.3–8 keV energy band. The HR is calculated for the detection where the off-axis angle was smallest if the source was detected multiple times.

(This table is available in its entirety in a machine-readable form in the online journal. A portion is shown here for guidance regarding its form and content.)

Others, like CX25, were detected closer on-axis in the new cycle 13 observations (6.′7 off-axis with six counts) but with many more counts in the observation reported in Jonker et al. (2011; 7.′2 off-axis with 48 counts) than in the new cycle 13 observation implying that the position provided in Jonker et al. (2011) will be more accurate. We do conclude that CX25 is variable in X-rays.

In total we detected 424 distinct sources in the area indicated with red circles and the red curved lines on the left side in Figure 1. The source list is given in Table 1 and the table provides information on α, δ, the error on α and δ, total number of counts detected, the observation ID of the observation resulting in the detection and the off-axis angle at which the source is detected. The errors on α and δ are the errors provided by WAVDETECT, and do not take into account the typical *Chandra* boresight uncertainty of 0.″6 (90%confidence). We do, however, add a column to Table 1 quoting the total uncertainty on the source position following formula (4) in Evans et al. (2010). For clarity, we repeat their equation here:

$$\log P = \begin{cases} 0.1145\theta - 0.4957 & \log C + 0.1932 \\ & \text{for } 0.0 < \log C < 2.1393 \\ 0.0968\theta - 0.2064 & \log C - 0.4260 \\ & \text{for } 2.1393 < \log C < 3.3 \end{cases},$$

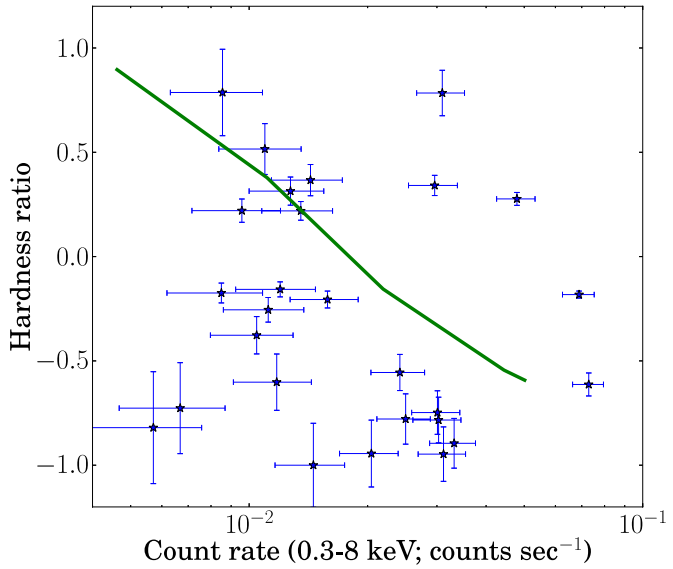

Figure 2. Hardness–intensity diagram for the 27 sources for which 20 or more counts were detected in *Chandra* cycle 13 observations for the GBS survey. To mitigate effects of small differences in exposure times we used count rates as a measure of intensity. The hardness is defined as the ratio between the count rate in the 2.5–8 keV minus that in the 0.3–2.5 keV band to the count rate in the full 0.3–8 keV energy band. Hard sources fall in the top half and soft sources in the bottom half of this figure. The green line shows the influence of the extinction ($N_{\rm H}$) on a power-law spectrum with index 2 for a source count rate of 0.05 counts s^{-1} and $N_{\rm H}$ values increasing from bottom right to top left from (0.01, 0.1, 1, 3, 10) $\times$ 10^{22} cm^{-2}.

(A color version of this figure is available in the online journal.)

where θ is the off-axis angle in arcminutes and C is the detected number of X-ray photons. The positional error P is given in arcseconds and it corresponds to a 95% confidence interval.

We provide individual *Chandra* source names, however, for briefness we use the source number in Table 1 preceded by "CXB" to indicate which source we discuss in this paper. For the error σ_N on the detected number of counts N, Grimm et al. (2005) give $\sigma_N = 1 + \sqrt{N + 0.75}$ after Gehrels (1986). To allow for a rough, easy calculation of the source flux based on the detected number of source counts we give the conversion factor for a source spectrum of a power law with photon index of 2 absorbed by $N_{\rm H} = 1 \times 10^{22}$ cm^{-2}: 7.76×10^{-15} erg cm^{-2} s^{-1} photon^{-1}.

2.2. X-ray Spectral Information

We extract source counts using circular source extraction regions of 10″. Background extraction regions are annulli with inner and outer radii of 15″ and 30″, respectively. We plot the 27 sources for which we detected 20 or more counts in a hardness–intensity diagram (Figure 2). To mitigate the effects that small differences in exposure time across our survey can have, we use count rates as a measure of intensity. We define the hardness ratio (HR) as the ratio between the count rate in the 2.5–8 keV minus that in the 0.3–2.5 keV band to the count rate in the full 0.3–8 keV energy band (after Kim et al. 2004). We derived the hardness using *XSPEC* version 12.7 (Arnaud 1996) by determining the count rates in the soft and hard band taking the response and ancillary response file for each of the sources. For these 27 sources photon pile-up is less than 10% even for the brightest source. Naively, one would expect most hard sources to be more distant and more absorbed than the soft sources, as the intrinsic spectral shape of the most numerous classes of sources we expect to find does not differ much.

The most interesting aspect from Figure 2 is perhaps the presence of three bright (rate $>2.5 \times 10^{-2}$ counts s^{-1}) and relatively hard sources (HR > 0). Their relatively hard spectrum makes it likely that these three sources (CXB3 [HR $= 0.28 \pm 0.03$], CXB6 [HR $= 0.78 \pm 0.11$], and CXB7 [HR $= 0.34 \pm 0.05$]) suffered significantly from X-ray absorption thus they are likely at a distance of more than 3 kpc, which, given their relatively high X-ray flux, means that their X-ray luminosity is substantial. CXB3 is probably a transient source (see below) and none of the three sources is associated with archival radio emission (see below) decreasing the chance that they are background active galactic nuclei (AGNs), and making them potential X-ray binaries.

As foreseen, the spectral information is insufficient for source classification for the majority of the total number of detected sources, therefore, classification will have to come from (multi-epoch) multi-wavelength observations. Finally, there seems to be a dichotomy in the hardness with one peak centered on a hardness of 0.2 and another centered on -0.8 with a paucity of sources with hardness 0. A similar dichotomy was reported in Warwick et al. (2011) and Jonker et al. (2011); see the latter paper for a possible explanation for the nature of this dichotomy.

2.3. Chandra Light Curves of Source CXB#1–10

We inspect the *Chandra* light curves of source CXB#1–10. We rebinned the light curves in 200 s bins. Sources CXB#1, 2, 3, 6, and 9 show suggestive evidence for flare-like variability. Fitting the light curve with a constant gives a χ^2 value of 16 (for 10 degrees of freedom (dof)), 35.9 (9 dof), 19.5 (10 dof), 18 (10 dof), 16.4 (9 dof), respectively. The light curves of source CXB# 4, 5, 7, 8, and 10 are consistent with being constant with χ^2 values of 8.4 (10 dof), 7.5 (9 dof), 11 (10 dof), 10 (9 dof), and 3.8 (10 dof), respectively. We do note that the number of counts in each 200 s bin varies between 35 and 3 counts between these sources and as a function of time. Therefore, certainly for the bins containing only a few counts the use of the χ^2 statistic is suspect. The small number of counts per bin in several cases makes it likely that some of the high values of reduced χ^2 are occurring due to chance fluctuations.

In Figure 3 we plot the light curves of the sources for which there is evidence for variability during the observations (i.e., CXB1, CXB2, CXB3, CXB6, and CXB9) and for comparison we plot in the top panel of the same figure the light curve of CXB10 for which our current data provides no evidence that the source varies during the observation.

3. DISCUSSION

Using 63 *Chandra* observations we cover the remaining ≈quarter of the 12 square degrees that comprise the GBS (Jonker et al. 2011). In this paper we provide the list of 424 X-ray sources that we find in this area and that have three or more counts in the short (2 ks) *Chandra* observations.

In total we detected 1640 unique X-ray sources. Of these, 875 are detected at Galactic latitudes below the plane and 765 at Galactic latitudes above the plane. For a symmetric distribution of 1640 sources one would expect 820 ± 20 on either side, making the detected distribution marginally skewed. We investigated the nature of this asymmetry by dividing the number of sources over the four quadrants in which they were detected. We made quadrants according to the Galactic coordinates of the

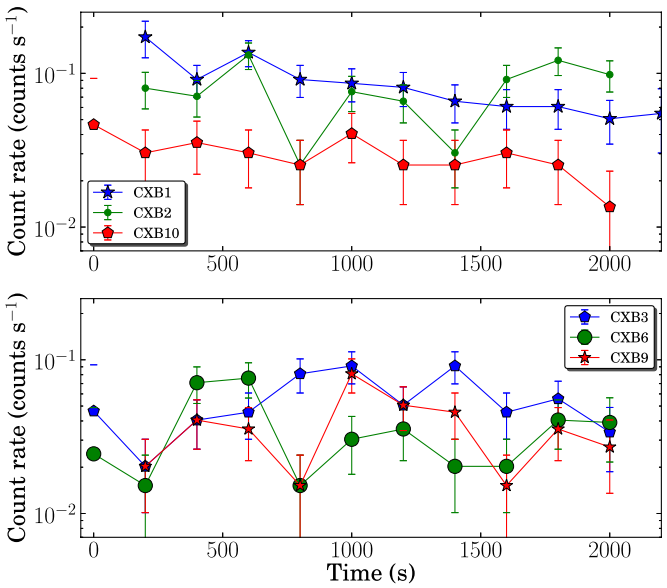

Figure 3. *Chandra* X-ray light curves of six CXB sources. Each point is an average of 200 s of *Chandra* data. For five sources there is suggestive evidence that the source is variable during the *Chandra* observation (CXB1, CXB2, CXB3, CXB6, and CXB9). For comparison we also plot in the top panel the light curve of CXB10 for which we find no evidence that the source varied during the observation.

(A color version of this figure is available in the online journal.)

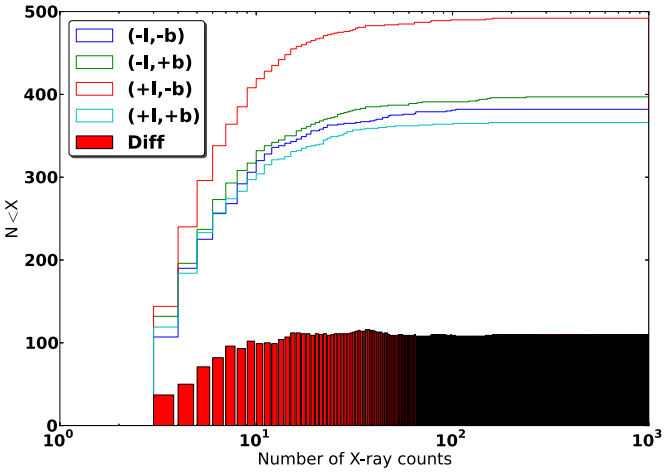

Figure 4. Cumulative distribution of the number of X-ray sources as a function of the number of source X-ray counts discovered in the GBS for four different quadrants according to the Galactic coordinates of the sources $(-l, -b)$, $(-l, +b)$, $(+l, +b)$, and $(+l, -b)$. The full histogram shows the cumulative difference in the number of X-ray sources as a function of the number of detected source X-rays found in the $(+l, -b)$ and the $(-l, -b)$ quadrants. The difference is qualitatively the same when comparing the number of X-ray sources in $(+l, -b)$ to the numbers in the other quadrants. There is a clear excess of number of X-ray sources discovered in the $(+l, -b)$ quadrant when compared with the other quadrants. The difference increases with X-ray count rate up to sources with $\lesssim$10 X-ray counts per source.

(A color version of this figure is available in the online journal.)

source and we counted the number of sources in each quadrant $(-l, -b$: #382), $(-l, +b$: #399), $(+l, +b$: #366) and $(+l, -b$: #493). It turns out that the quadrant $(+l, -b)$ is responsible for the apparent asymmetry in the number of detected sources (see Figure 4).

Most of the sources we expected to detect are relatively nearby (within 3 kpc; Jonker et al. 2011), nevertheless, the different average extinction in the GBS areas in the four quadrants could

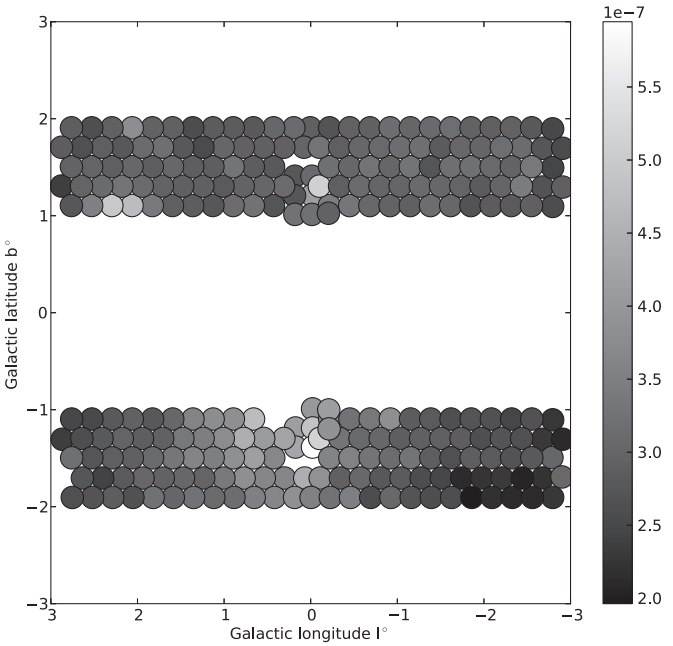

Figure 5. Background count rate (pixel^{-1} s^{-1}) as measured by *Chandra*. The background is higher in the $(+l, -b)$ part of the GBS area than in the other areas. We removed two observations from this plot—one where we used the FAINT event mode which does not allow for the thorough cleaning of cosmic-ray afterglow events and therefore yields a much higher background and one where the background is artificially increased due to the presence of a very bright X-ray source.

still have a significant influence on the number of detected sources. The average extinction is indeed lower in the $(+l, -b)$ quadrant where we detected most of the new X-ray sources (see the right panel of Figure 1). The overdensity of sources we find in quadrant $(+l, -b)$ of the GBS area coincides with the presence of diffuse X-ray-emitting gas in that part of the GBS area, as found by *ROSAT* (Snowden et al. 1997).

In order to investigate this asymmetry further we compared the different background levels in our *Chandra* observations as determined by the WAVDETECT tool (see Figure 5; a higher background is indicated by a lighter shade of gray). The background levels could influence the detection probability especially for sources with three counts falling far away from the optical axis of the satellite. The diffuse emission could show up as a diffuse number of pixels with one or two counts or in areas with a lower extinction a larger amount of one- and two-count sources such as RS CVn, and coronally active stars might be present.

For a background count rate per pixel per second of $\approx 5 \times 10^{-7}$ (see Figure 5) and 2 ks exposures and $\lesssim$100 pixels for the point-spread function far off-axis, the expected background rate is $\lesssim$0.1 count per 2 ks observation in such an area. Whereas there is indeed a difference in the background count rate in line with the expectation from either more one- to two-count point sources or more diffuse emission in the $(+l, -b)$ quadrant of the GBS area, this enhanced background does not have a large effect on the number of three-count sources even far off-axis.

We conclude that the overdensity of sources in the $(-l, +b)$ part of our GBS area is likely caused by the lower average extinction in that quadrant of the GBS survey area, whereas the higher X-ray background in that area is in line with the diffuse gas as found by Snowden et al. (1997). Those authors argued that this diffuse gas is at the distance of the bulge.

3.1. Comparison with ROSAT Sources

In order to investigate whether sources in our CXB source list are detected by *ROSAT* we cross-correlated the GBS CXB source list with the *ROSAT* All Sky Survey (RASS; Voges et al. 1999). We queried both the Bright as well as the Faint catalog, the *ROSAT* High Resolution Imager (HRI) Pointed Observations (1RXH), and the Second *ROSAT* Position Sensitive Proportional Counter (PSPC) Catalog (2RXP) using the VizieR database. To accommodate the relatively large positional uncertainties in many of the *ROSAT* source detections, we searched for *ROSAT* sources within 30″ of the *Chandra* positions of our CXB sources.

We find two RASS (faint) sources that have a position relatively close to the GBS CXB sources CXB9 and CXB11. These sources are probably associated with the *ROSAT* sources 1RXS J174916.5−311509 and 1RXS J175019.0−302654, respectively. CXB9 is 9.″3 away from 1RXS J174916.5−311509. CXB9 is also associated with an O8 III *Tycho*-2 source (Hynes et al. 2012; see their work for further details on this source). CXB11 is 22″ away from 1RXS J175019.0−302654 which is probably the same source as 2RXP J175020.0−302616. We furthermore find that CXB55 likely corresponds to 1RXH J175017.6−311427 (reported in Rappaport et al. 1994). The angular distance between the two sources is 12.″2. Finally, CXB93 might be related to 1RXH J174612.7−320637 which is located at an angular separation of 25″.

3.2. Transient Sources

The first three CXB sources (CXB1–3) are bright enough that they should have been detected in RASS if they were as bright during RASS as they were in our *Chandra* observations. However, they were not detected in RASS, and thus we are inclined to conclude that their X-ray luminosity has significantly varied between our *Chandra* and the RASS observation. Before we could firmly conclude that these sources are variable, we verified the *Chandra* X-ray spectrum of each of these sources. CXB1 and CXB2 have spectra that should have allowed for a detection in RASS, however, we found that the spectrum of CXB3 is strongly absorbed, potentially providing an explanation as to why *ROSAT* did not detect the source. Using *C*-statistics we fit a spectral model consisting of a power law absorbed by interstellar material to the X-ray spectrum. For CXB3 we find a best fit $N_{\rm H} = (2.7 \pm 0.9) \times 10^{22}$ cm^{-2} for a power-law index of 2.4 ± 0.7. Extrapolating this model to the *ROSAT* band (0.01–2.5 keV) we find that the source flux is 2.5×10^{-12} erg cm^{-2} s^{-1}. This implies that the source should have been detected by RASS although we note that the extrapolation to low energies carries a significant uncertainty. We tentatively conclude that CXB1, 2, and 3 are transient or at least highly variable sources.

CXB3 has a bright NIR counterpart at $K = 10.06 \pm 0.04$ (2MASS J17461440−3219494; this 2MASS source was not picked up in our cross-correlation with SIMBAD; see Section 4) at an angular distance of 0.″13, which is consistent with the 95% confidence uncertainty on the position of the source of 0.″31 (see Table 1). The extinction toward the source as given by Gonzalez et al. (2012) is $E(B-V) \sim 2.8$. This yields an $N_{\rm H} \sim 1.6 \times 10^{22}$ cm^{-2} which is consistent within the uncertainties with the value we find from our fit to the X-ray spectrum (using the conversion of $E(B-V)$ to A_V using a gas to dust ratio of $R = 3.1$ and the conversion from A_V to $N_{\rm H}$ from Predehl & Schmitt 1995). This value for the extinction is also consistent with a distance to the source of ∼8 kpc. For that distance the source luminosity will be around 6×10^{33} erg s^{-1}. The source is also detected in the 2MASS, *Wide-field Infrared Survey Explorer* (*WISE*), and GLIMPSE surveys (Skrutskie et al. 2006; Wright et al. 2010; Benjamin et al. 2003; Churchwell et al. 2009, respectively) as well as in our Blanco/DECam r' data at $r' \sim 19.8$ (C. B. Johnson et al., in preparation). Correcting for the reddening of Gonzalez et al. (2012) we find that the spectral energy distribution fits well with the Kurucz model (Castelli & Kurucz 2003) of a late-K red giant of $T_{\rm eff} = 4000$ K and $\log g = 1.5$. This source is a candidate symbiotic X-ray binary (see Hynes et al. 2014).

We also investigated whether *ROSAT* sources found using RASS (Bright and Faint catalogs) as well as pointed observations (from the HRI and the PSPC) fell in the observed GBS CXB area but were not detected. We used TOPCAT to cross-correlate the VizieR *ROSAT* Catalogues mentioned above with the coordinates of the *Chandra* pointing centers. We considered a sky area of 7′ around the *Chandra* pointing centers in this cross-correlation. The resulting list contains all the *ROSAT* sources that fall inside this sky area. We remove the *ROSAT* sources that have an associated GBS CXB counterpart within 30″ (see above). Below we discuss the *ROSAT* sources that were no longer detected in the GBS CXB observations.

1RXH J174423.1−320254 and 1RXH J174449.9−321701 have no CXB counterpart within 30″, however, both sources were detected by *ROSAT* at signal-to-noise ratios of only 3 and 2.7, respectively. The Second *ROSAT* PSPC Catalog source 2RXP J175138.6−295024 also went undetected in the CXB. The false alarm probability for the *ROSAT* detection of this source is 1.2×10^{-2}.

There are 15 sources from the RASS Faint source catalog within 7′ of a *Chandra* CXB pointing that do not have a CXB counterpart within 30″ (see Table 2). However, we note that the uncertainty on the position of the faint RASS sources ranges between 14″–49″ and the search radius of 30″ might be too strict. However, enlarging the matching radius provides other problems. For example, for a search radius of 1′, 1RXS J174608.8−320544 has two potential CXB counterparts:

Table 2
RASS Faint Sources without CXB X-Ray Counterparts within 30″

1RXS	R.A.	Decl.	Δ (″)	*L*
J175237.6−294714[a]	268.1567	−29.78722	49	9
J175343.3−291444	268.4304	−29.2457	16	8
J175342.4−290809	268.4267	−29.1358	19	10
J175420.8−285412	268.5867	−28.9033	15	12
J175606.4−283311	269.0267	−28.5532	30	8
J175712.8−280510	269.3033	−28.0863	17	10
J175836.1−273358	269.6504	−27.5661	19	8
J175050.7−301735	267.7112	−30.2932	37	7
J175323.2−295649	268.3467	−29.9471	19	8
J175334.9−295013	268.3954	−29.8369	14	8
J175421.9−292206	268.5913	−29.3683	14	15
J175855.9−272945	269.7329	−27.4960	27	9
J175019.0−304843	267.5792	−30.8119	30	10
J174906.7−311915	267.2779	−31.3208	21	11
J174608.8−320544[a]	266.5367	−32.0956	25	17

Notes. Δ is the uncertainty on the source position provided by the RASS. *L* is the likelihood of source detection $L = -\ln(1-P)$, where *P* is the probability that the source is real. Those sources with $L \gtrsim 9$ that went undetected in the GBS are good candidate transients.
[a] Marked in the RASS as a potentially extended *ROSAT* source.

Table 3
NVSS Sources Close to CXB X-Ray Sources

CXB#	NVSS	R.A. (J2000)	Decl. (J2000)	ΔR.A. (s)	ΔDecl. (″)	S1.4 (mJy)	Separation (″)
CXB19	175737−281000	17 57 37.72	−28 10 00.7	0.38	9.4	3.8 ± 0.6	7.9
CXB23	175230−300107	17 52 30.97	−30 01 07.8	0.03	0.6	350 ± 10	0.95
CXB28	175205−303026	17 52 05.68	−30 30 26.7	0.43	6.7	2.8 ± 0.5	3.6
CXB127	174748−312315	17 47 48.62	−31 23 15.2	0.04	0.6	540 ± 15	5.0
CXB150	175233−295645	17 52 33.16	−29 56 45.5	0.03	0.6	235 ± 10	0.71
CXB162	173357−302729	17 33 57.85	−30 27 29.2	0.14	1.9	8.3 ± 0.5	1.37
CXB163	173229−302522	17 32 29.34	−30 25 22.7	0.62	8.6	2.4 ± 0.6	17.9
CXB288	173251−302919	17 32 51.74	−30 29 19.4	0.05	0.7	35 ± 1.2	1.1
CXB384	174857−310445	17 48 57.10	−31 04 45.4	0.46	8.3	5.5 ± 0.7	3.5

CXB93 and CXB406. CXB93 is at 57.″2 and CXB406 lies at 51.″6 from 1RXS J174608.8−320544 (CXB93 and CXB406 are 94.″7 apart and they are thus not consistent with being the same source). Interestingly, given that 1RXS J174608.8−320544 is marked as a potentially extended source in the RASS catalog, it might be that the source is a blend of CXB93 and CXB406.

For all the sources with $L \gtrsim 9$ in Table 2 as well as the two 1RXH sources and the one 2RXP source not detected in CXB, it is conceivable that the *ROSAT* observations found the source in a bright state and/or that the source spectrum is too soft to allow for a detection in the GBS CXB observations. Several sources present secure *ROSAT* detections and they should have been detected in our CXB observations, e.g., 1RXS J175421.9−292206 is detected at more than 5σ significance with *ROSAT* hardness ratio 1 (HR1) = 0.43 ± 0.37 and hardness ratio 2 (HR2) = 0.22 ± 0.42. Here, HR1 = $(B - A)/(B + A)$ and HR2 = $(D - C)/(D + C)$, with A = 0.11–0.41 keV, B = 0.52–2.0 keV, C = 0.5–0.9 keV, and D = 0.9–2.0 keV count rate. Therefore, the X-ray spectrum is not too soft for *Chandra*, indicating that this source has varied between the *ROSAT* and the *Chandra* observations. For some other sources, most notably those with $L \lesssim 9$ in Table 2, the *ROSAT* detection significance is also so low that they could be spurious detections.

4. RADIO NVSS DETECTIONS AND SIMBAD LISTING OF GBS CXB SOURCES

After Maccarone et al. (2012) we provide the result from the cross-correlation between the CXB source list and the NRAO VLA Sky Survey (NVSS), where NRAO and VLA stand for National Radio Astronomy Observatory and Very Large Array, respectively. We considered sources within 30″ of a CXB source as a likely match. Table 3 contains the nine NVSS sources we find and their likely CXB counterparts.

The three radio-bright objects associated with CXB23, CXB127, and CXB150 are also detected in Nord et al. (2004) as 330 MHz sources called GCPS 359.845−1.845 (Δ = 3.″8; $S_{330\,\mathrm{MHz}}$ = 764 mJy), GCPS 358.154−1.680 (Δ = 17″; $S_{330\,\mathrm{MHz}}$ = 1464 mJy), and GCPS 359.912−1.815 (Δ = 3.″6; $S_{330\,\mathrm{MHz}}$ = 474 mJy), respectively. For $S_\nu \propto \nu^\alpha$, where ν is the radio frequency and S_ν is the radio flux, this yields $\alpha = -0.5, -0.7, -0.5$, respectively. These sources have radio spectra consistent with being AGNs and we thus preliminary classify CXB23, CXB127, and CXB150 as such.

For the other GBS CXB sources with potential radio counterparts it is more difficult to provide a classification on the basis of the potential association with the radio source alone.

Finally, we cross-correlated the positions of the CXB sources with the entries in SIMBAD where we retained optical sources that have a position within 5″ of that of a CXB source and radio and X-ray sources that have a position within 30″ from a CXB source. Table 4 contains the resulting list of sources. Some of the NVSS sources are not found this way (compare with Table 3) whereas others are (e.g., the match between the NVSS source and CXB23 is also found using SIMBAD). Many of the associations of CXB sources with bright optical counterparts were already found in Hynes et al. (2012). Note that some CXB sources have multiple entries as they have more than one potential counterpart within 5″, such as CXB93, CXB256, and CXB422, or they have multiple detections of presumably the same object with slightly different positions such CXB9, CXB23, and CXB150.

In order to estimate the number of false positive identifications, we then shifted all the CXB source positions by 15″or 30″ north or south, and we redid the cross-correlation. On average, we get 5.5 SIMBAD matches and almost all of these spurious matches are Optical Gravitational Lensing Experiment (OGLE) sources, with a few matches to stars from the open cluster NGC 6451. Thus, we therefore conclude that ∼38 of our 43 optical/IR matches are real matches, with the OGLE matches being subject to the highest false alarm probability.

From Table 4, we find three cataclysmic variables with close positional matches to the CXB X-ray source positions (CXB10, CXB26, and CXB245). These associations are probably all real. Finally, CXB97 is well matched with a W UMa type source. This is likely to be a real match, and part of the predicted W UMa population.

5. SUMMARY

In this paper we have presented the *Chandra* source list and some properties of the X-ray sources of observations covering the ≈quarter of the total survey area of 12 square degrees remaining to be done after the work of Jonker et al. (2011). This paper thus completes the *Chandra* survey part of the GBS. The accurate *Chandra* source positions will help identify the optical, NIR, and UV counterparts. The 424 X-ray sources that have been discovered here, together with the 1216 unique sources from Jonker et al. (2011), compare well with the total number of ≈1650 X-ray sources that we predicted we should detect in the full 12 square degrees. However, this is of course no guarantee that the number of sources per source class is close to the number we calculated. Optical and NIR photometry including variability information and spectroscopy is necessary to determine the nature of each of the sources (see for instance Ratti et al. 2013; Britt et al. 2013; Hynes et al. 2014; Torres et al. 2013).

Table 4
Optical or Near-infrared Sources Found in the SIMBAD Data Base within 5″ of CXB X-ray Sources

CXB#	CXB#	R.A. J2000−CXB	Decl. J2000−CXB	Angular D	Simbad Name	R.A. J2000	Decl. J2000	ID
1	CXB2	268.499460	−29.4852781	7.2	AX J1754.0−2929	268.500000	−29.483333	X
2	CXB5[a]	263.0362304	−30.474635	0.2	HD 315961	263.036154	−30.474636	K5
3a	CXB9[a]	267.3192035	−31.2550666	0.6	HD 161853	267.319017	−31.255022	O8 III
3b	CXB9	267.3192035	−31.2550666	3.4	PN RPZM 40	267.319583	−31.254167	PN?
3c	CXB9	267.3192035	−31.2550666	10	1RXS J174916.5−311509	267.318671	−31.252244	X
4	CXB10	269.6350093	−27.8789043	0.7	MACHO 401.48296.2600	269.635208	−27.879000	CV
5	CXB11	267.5862652	−30.4477944	22	1RXS J175019.0−302654	267.579158	−30.448469	X
6	CXB17[a]	268.6255656	−29.3992464	0.2	2MASS J17543011−2923572	268.625488	−29.399244	IR
7	CXB21	268.7011304	−29.3277772	3.7	OGLE BUL-SC4 568004	268.700458	−29.328611	V*
8a	CXB23	268.1288255	−30.0186408	0.6	[IBR2011] J1752−3001	268.128960	−30.018515	Radio
8b	CXB23	268.1288255	−30.0186408	1.5	[LKL2000] 43	268.129167	−30.018333	Radio
8c	CXB23	268.1288255	−30.0186408	4.3	GCPS 111	268.130208	−30.018500	Radio
9	CXB26	268.4491784	−29.7439772	1.0	OGLE BUL-SC3 6033	268.448875	−29.743861	CV
10	CXB28	268.0240465	−30.5064844	2.1	2XMM J175205.6−303023	268.023375	−30.506556	X
11	CXB29	268.5549195	−29.4830887	0.6	OGLE BUL-SC4 155897	268.554750	−29.483028	V*
12	CXB34	266.8706341	−32.2448156	12	2MASS J17472806−3214462	266.866917	−32.246194	X
13	CXB36[a]	266.5600100	−32.1033654	4.1	LTT 7073	266.560160	−32.102233	PM* M2 V
14	CXB49	267.3703237	−31.3067944	0.8	2MASS J17492885−3118237	267.370225	−31.306603	Candidate YSO
15	CXB54	268.1172224	−29.9895816	13	RRF 9	268.114167	−29.987222	Radio
16	CXB55	267.5735447	−31.2430775	12	[RDL94] Terzan 6 A	267.574167	−31.239722	X
17	CXB58	268.5832235	−29.6379212	0.8	2MASS J17541996−2938157	268.583188	−29.637694	EB*
18	CXB63	267.6738181	−30.1941350	1.3	Cl* NGC 6451 KF 227	267.674208	−30.194250	in Cluster
19a	CXB93[a]	266.5529013	−32.1035349	2.5	LTT 7072	266.552088	−32.103529	PM* M2 V
19b	CXB93[a]	266.5529013	−32.1035349	3.7	** LDS 611/GJ 2130 C	266.553167	−32.102528	**
20	CXB97	269.7613953	−27.4890113	0.9	V* V1723 Sgr	269.761125	−27.488917	EB*WUMa
21	CXB100	268.4645298	−29.650292	2.3	OGLE BUL-SC3 769186	268.464292	−29.650889	V*
22	CXB112	263.2739071	−30.5863552	2.0	LP 920−61	263.274083	−30.585833	PM* M2.5
23	CXB116[a]	269.2814150	−27.1476849	0.4	HD 314886	269.281369	−27.147590	A5
24	CXB127	266.9509625	−31.3875612	3.0	NVSS J174748−312315	266.950958	−31.388389	Radio
25	CXB128[a]	266.7138646	−25.7794799	1.5	CD-25 12283	266.714287	−25.779338	F8
26a	CXB150	268.1381712	−29.9457729	0.7	VCS4 J1752−2956	268.137946	−29.945806	Radio
26b	CXB150	268.1381712	−29.9457729	3.5	GCPS 115	268.139292	−29.945750	Radio
27	CXB181[a]	268.73059000	−29.2027756	0.3	HD 162962	268.730569	−29.202854	A
28	CXB183	268.6757225	−28.8307272	3.0	IRAS 17515−2849	268.674792	−28.830500	Star
29	CXB200[a]	263.4644661	−30.8417862	0.5	TYC 7376−433−1	263.464475	−30.841914	Star
30	CXB211[a]	265.8693744	−32.2325220	2.6	HD 160826	265.870188	−32.232264	B9 V
31	CXB225[a]	269.0803986	−28.4701699	2.5	TYC 6853−3032−1	269.079825	−28.470642	Star
32	CXB233[a]	268.83897484	−28.5734201	1.1	HD 316692	268.839115	−28.573143	A0
33	CXB245	268.2919765	−29.3556874	0.5	OGLE J175310.04−292120.6	268.291833	−29.355722	Dwarf Nova
34a	CXB256	267.7514663	−30.3199539	1.7	Cl* NGC 6451 PMR 65	267.751250	−30.319528	in Cluster
34b	CXB256	267.7514663	−30.3199539	1.7	Cl* NGC 6451 PMR 64	267.751917	−30.319667	in Cluster
35	CXB287[a]	263.3901785	−30.534113	1.5	HD 158982	263.389732	−30.533990	A2 IV/V
36	CXB293	268.710370	−29.3371961	0.4	2MASS J17545048−2920142	268.710375	−29.337306	EB*
37	CXB302[a]	269.6706800	−27.9024008	0.3	TYC 6849−1627−1	269.670621	−27.902478	Star
38	CXB306[a]	269.5399321	−28.1418302	0.4	HD 163613	269.539931	−28.141712	B1 Iab
39	CXB352	268.4262642	−29.8320194	1.3	OGLEII DIA BUL-SC3 5152	268.426333	−29.831667	EB*
40	CXB361	268.1649063	−29.752345	5.0	OGLE BUL-SC37 441760	268.163375	−29.751944	V*
41	CXB366	268.1003203	−29.7169994	0.2	2MASS J17522407−2943013	268.100292	−29.717056	EB*
42	CXB380	267.3212976	−31.2837757	11.5	SNR G358.4−01.9	267.325000	−31.283333	SNR
43a	CXB422[a]	262.8208422	−30.3215429	0.8	HD 315956	262.820644	−30.321404	F2
43b	CXB422[a]	262.8208422	−30.3215429	3.2	[RHI84] 9−186	262.820125	−30.320917	M4

Notes. Radio or X-ray sources found in the SIMBAD database within 30″ of CXB X-ray sources. Angular *D* stands for the angular distance between the SIMBAD and the CXB source position. PM* means high proper motion star, EB* stands for eclipsing binary star. V* denotes variable star and ** means double or multiple star. PN stands for planetary nebula and YSO for young stellar object. Finally, supernova remnant is abreviated as SNR and cataclysmic variable as CV.
[a] Association already found in Hynes et al. (2012).

We discussed the apparent overdensity of sources in the $(+l, -b)$ quadrant of the GBS area. We conclude that this is caused by the lower extinction in this quadrant.

We compared our source list with that of RASS. Furthermore, we compared our *Chandra* source list with the sources found in the catalog of sources derived from pointed HRI and PSPC *ROSAT* observations that fall inside the GBS area. Finally, we investigate whether some of the sources we report on here are present in public radio surveys.

The authors thank the CXC for scheduling the *Chandra* observations. R.I.H., C.T.B., and C.B.J., acknowledge support from the National Science Foundation under grant No. AST-0908789. This research has made use of the SIMBAD database,

operated at CDS, Strasbourg, France. This research has made use of the VizieR Catalogue access tool, CDS, Strasbourg, France. The original description of the VizieR service was published in A&AS, 143, 23. This publication makes use of data products from the *Wide-field Infrared Survey Explorer*, which is a joint project of the University of California, Los Angeles, and the Jet Propulsion Laboratory/California Institute of Technology, funded by the National Aeronautics and Space Administration (NASA). This work is based in part on observations made with the *Spitzer Space Telescope*, which is operated by the Jet Propulsion Laboratory, California Institute of Technology under a contract with NASA.

REFERENCES

Arnaud, K. A. 1996, in ASP Conf. Ser. 101, Astronomical Data Analysis Software and Systems V, ed. G. H. Jacoby & J. Barnes (San Francisco, CA: ASP), 17
Belczynski, K., & Taam, R. E. 2004, ApJ, 603, 690
Belczynski, K., Wiktorowicz, G., Fryer, C. L., Holz, D. E., & Kalogera, V. 2012, ApJ, 757, 91
Benjamin, R. A., Churchwell, E., Babler, Brian L., et al. 2003, PASP, 115, 953
Britt, C. T., Torres, M. A. P., Hynes, R. I., et al. 2013, ApJ, 769, 120
Castelli, F., & Kurucz, R. L. 2003, in Modelling of Stellar Atmospheres, New Grids of ATLAS9 Model Atmospheres, ed. N. Piskunov et al. (IAU Symposium, Vol. 210; San Francisco, CA: ASP), A20
Churchwell, E., Babler, B. L., Meade, M. R., et al. 2009, PASP, 121, 213
Evans, I. N., Primini, F. A., Glotfelty, K. J., et al. 2010, ApJS, 189, 37
Farr, W. M., Sravan, N., Cantrell, A., et al. 2011, ApJ, 741, 103
Fryer, C. L., Belczynski, K., Wiktorowicz, G., et al. 2012, ApJ, 749, 91
Garmire, G. P. 1997, BAAS, 29, 823
Gehrels, N. 1986, ApJ, 303, 336
Gonzalez, O. A., Rejkuba, M., Zoccali, M., et al. 2012, A&A, 543, A13
Greiss, S., Steeghs, D., Jonker, P. G., et al. 2014, MNRAS, in press (arXiv:1312.2958)
Grimm, H., McDowell, J., Zezas, A., Kim, D., & Fabbiano, G. 2005, ApJS, 161, 271
Hong, J. S., van den Berg, M., Grindlay, J. E., & Laycock, S. 2009, ApJ, 706, 223
Hynes, R. I., Wright, N. J., Maccarone, T. J., et al. 2012, ApJ, 761, 162
Hynes, R. I., Torres, M. A. P., Heinke, C. O., et al. 2014, ApJ, 780, 11
Ivanova, N., Justham, S., Chen, X., et al. 2013, A&ARv, 21, 59
Jonker, P. G., Bassa, C. G., Nelemans, G., et al. 2011, ApJS, 194, 18
Kiel, P. D., & Hurley, J. R. 2006, MNRAS, 369, 1152
Kim, D., Cameron, R. A., Drake, J. J., et al. 2004, ApJS, 150, 19
King, A. R., & Ritter, H. 1999, MNRAS, 309, 253
Kreidberg, L., Bailyn, C. D., Farr, W. M., & Kalogera, V. 2012, ApJ, 757, 36
Lasota, J.-P. 2008, NewAR, 51, 752
Lee, C.-H., Brown, G. E., & Wijers, R. A. M. J. 2002, ApJ, 575, 996
Maccarone, T. J., Torres, M. A. P., Britt, C. T., et al. 2012, MNRAS, 426, 3057
Murray, S. S., Kenter, A., Forman, W. R., et al. 2005, ApJS, 161, 1
Narayan, R., & McClintock, J. E. 2005, ApJ, 623, 1017
Nord, M. E., Lazio, T. J. W., Kassim, N. E., et al. 2004, AJ, 128, 1646
Özel, F., Psaltis, D., Narayan, R., & McClintock, J. E. 2010, ApJ, 725, 1918
Özel, F., Psaltis, D., Narayan, R., & Santos Villarreal, A. 2012, ApJ, 757, 55
Pfahl, E., Rappaport, S., & Podsiadlowski, P. 2002, ApJL, 571, L37
Predehl, P., & Schmitt, J. H. M. M. 1995, A&A, 293, 889
Rappaport, S., Dewey, D., Levine, A., & Macri, L. 1994, ApJ, 423, 633
Ratti, E. M., van Grunsven, T. F. J., Jonker, P. G., et al. 2013, MNRAS, 428, 3543
Schlegel, D. J., Finkbeiner, D. P., & Davis, M. 1998, ApJ, 500, 525
Shahbaz, T., & Kuulkers, E. 1998, MNRAS, 295, L1
Skrutskie, M. F., Cutri, R. M., Stiening, R., et al. 2006, AJ, 131, 1163
Snowden, S. L., Egger, R., Freyberg, M. J., et al. 1997, ApJ, 485, 125
Torres, M. A. P., Jonker, P. G., Britt, C. T., et al. 2013, arXiv:1310.0224
Udalski, A., Kowalczyk, K., Soszynski, I., et al. 2012, AcA, 62, 133
Voges, W., Aschenbach, B., Boller, Th., et al. 1999, A&A, 349, 389
Wang, Q. D., Gotthelf, E. V., & Lang, C. C. 2002, Natur, 415, 148
Warwick, R. S., Pérez-Ramírez, D., & Byckling, K. 2011, MNRAS, 413, 595
Weisskopf, M. C., Brinkman, B., Canizares, C., et al. 2002, PASP, 114, 1
Wright, E. L., Eisenhardt, P. R. M., Mainzer, A. K., et al. 2010, AJ, 140, 1868
Wu, Y. X., Yu, W., Li, T. P., Maccarone, T. J., & Li, X. D. 2010, ApJ, 718, 620